An analysis of degradation phenomena in polymer electrolyte membrane water electrolysis

Christoph Rakousky [a], Uwe Reimer [a], Klaus Wippermann [a], Marcelo Carmo [a, *], Wiebke Lueke [a], Detlef Stolten [a, b]

[a] Forschungszentrum Jülich GmbH, IEK-3: Electrochemical Process Engineering, 52425 Jülich, Germany
[b] Chair for Fuel Cells, RWTH Aachen University, Germany

HIGHLIGHTS

- Durability of state-of-the-art PEM electrolysis tested for just over 1000 h.
- Reversible voltage increase recovers immediately after brief shut downs.
- Titanium contamination of electrodes and observed growth of Pt particles.
- Cell assembly highly affects results of CCM durability testing.
- Pt-coated PTL reduces degradation by 89%.

ARTICLE INFO

ABSTRACT

The durability of a polymer electrolyte membrane (PEM) water electrolysis single cell, assembled with regular porous transport layers (PTLs) is investigated for just over 1000 h. We observe a significant degradation rate of 194 $\mu V\ h^{-1}$ and conclude that 78% of the detectable degradation can be explained by an increase in ohmic resistance, arising from the anodic Ti-PTL. Analysis of the polarization curves also indicates a decrease in the anodic exchange current density, j_0, that results from the over-time contamination of the anode with Ti species. Furthermore, the average Pt-cathode particle size increases during the test, but we do not believe this phenomenon makes a significant contribution to increased cell voltages. To validate the anode Ti-PTL as a crucial source of increasing resistance, a second cell is assembled using Pt-coated Ti-PTLs. This yields a substantially reduced degradation rate of only 12 $\mu V\ h^{-1}$, indicating that a non-corroding anode PTL is vital for PEM electrolyzers. It is our hope that forthcoming tailored PTLs will not only contribute to fast progress on cost-efficient stacks, but also to its long-term application of PEM electrolyzers involved in industrial processes.

© 2016 Elsevier B.V. All rights reserved.

1. Introduction

'Green' electricity generated from renewable but intermittent sources (such as wind turbines and photovoltaics) can be stored in the form of hydrogen produced using polymer electrolyte membrane (PEM) water electrolyzers [1,2]. However, the widespread and cost-effective implementation of PEM water electrolysis as a means of storing electrical energy will only be possible when PEM electrolyzers can achieve lifetimes on the order of 50,000 to 100,000 h [3]. Unfortunately, to date the scientific community has

devoted very little attention to understanding the degradation mechanisms of cell and stack components. From the few studies of this topic that have been published, three main phenomena can be highlighted:

  i) Passivation of Ti-based components on the anode side over time.
 ii) Deactivation of electrolyte and electrode performance due to ion impurities in the feed water.
iii) Structural changes to the catalyst material.

With respect to i): Over time, high applied anode overpotentials facilitate the passivation of the Ti based components [4—7], leading

to an increase in ohmic cell resistance and a subsequent increase of the cell voltage [4]. Pt-based and Au-based coatings are normally used to circumvent this passivation issue with bipolar plates [4,5,8,9]. However, the passivation of the Ti based porous transport layer (PTL) is only rarely taken into account [10–13] and the influence of a protective coating on performance degradation has yet to be fully quantified. Unfortunately, the protective coatings have a major impact on investment costs. In order to find new and cost efficient alternatives, the degradation mechanisms must be better understood and/or defined when using conventional Ti-PTL.

Regarding ii): Ion impurities present in the feed water (Fe, Cr, Cu, Na, etc.) were shown to accumulate in the catalyst-coated membrane (CCM), where they decrease the conductivity of the ionomer and electrode performance [14–20]. These effects relate to increased ohmic and charge transfer resistances [15] and were shown to be reversible when reactivating the CCM in sulfuric acid [14,15].

Finally, in the case of iii): As was shown ex situ, iridium active components can dissolve at high anode potentials, especially when the working electrode potential is varied [21,22]. However, at constant potential the effect of dissolution seems to be negligible [21]. During a long-term test, a reduction in the anode's catalyst area was associated with a decrease in the double layer capacitance and an increase in the charge transfer resistance [23]. Voltage cycling has also been shown to affect the cathode, where it facilitates the reduction of the electrochemically-active surface area (ECSA) of the platinum nanoparticles [24].

In this manuscript, durability profiles of single PEM electrolysis cells running under conventional operating conditions (80 °C, 2 A cm^{-2}) were obtained using both coated and uncoated commercial Ti-PTLs. Moreover, in order to relate the degradation mechanism to the Ti-PTL alone, all cell components and peripherals were protected against corrosion and the leaching out of metal ions, which would cause the membrane to critically degrade over time. Additionally, reproducible and efficient state-of-the-art commercial CCMs from Greenerity GmbH were used to reach meaningful conclusions.

2. Experimental

An electrolysis cell was operated at a constant current density of 2 A cm^{-2} for a period of about 1000 h (6 weeks), with an extension of 65 h, as can be seen in Fig. 1. Electrochemical and physical
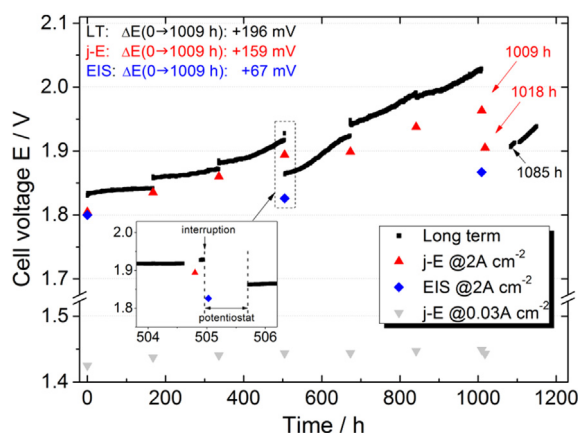
Fig. 1. Cell voltage at 80 °C during long-term operation at 2 A cm^{-2} (black squares). Triangles indicate the cell voltages during polarization curves (j–E) at 2 A cm^{-2} (upward) and 0.03 A cm^{-2} (downward). The times where EIS spectra were recorded and the cell voltages during the initial conditioning phase for the EIS measurements at 2 A cm^{-2} are marked with diamonds.

characterization methods were employed before, during and after the test in order to understand the long-term behavior of single cells and to locate the specific components undergoing degradation.

2.1. CCM and cell setup

The CCM samples tested were products by Greenerity GmbH. The anode catalyst layer contained IrO_2 and TiO_2 with an Ir-loading of 2.25 mg cm^{-2}. Pt/C was used as the cathode catalyst at a Pt loading of 0.8 mg cm^{-2}, while a Nafion® 117 membrane was used as the electrolyte. Two sheets of Toray paper (TGP-H 120) with a total thickness of 700 μm were used as the cathode PTL. Porous titanium sinter plates (GKN T3P, 42 × 42 × 1.3 mm) were used as anode PTL and will be referred to hereinafter as Ti-PTL. Platinum-coated titanium bipolar plates with serpentine-type flow fields were used on both sides, that on the cathodic side also being gold-plated. PTFE and silicone gaskets sealed the cell with an active area of 17.64 cm^2.

The half-cell potentials of the anodic and cathodic bipolar plates were recorded with respect to a dynamic hydrogen reference electrode (DHE) [25–28]. For this purpose, two platinum wires (0.1 mm diameter, Alfa Aesar) were hot pressed on the cathode side of the CCM using a strip of Nafion 212 membrane for fixing. The wires were placed in a parallel configuration (with a spacing of about 3 mm) in the catalyst-free area of the CCM, such that their tips were located about 3 mm from the edge of the catalyst-coated area. An electric current (DHE-current) of 12 μA was passed through the two wires to maintain constant hydrogen coverage of the negatively polarized Pt-wire, which was then used as the reference electrode. The voltage between the Pt wires (DHE-voltage) increased upon DHE start-up and reached a constant value after about 30 min. All half-cell potentials were then recorded after 60 min of continuous DHE operation. Due to instrument availability, no half-cell potentials are available before 210 h.

2.2. Test bench and long-term testing

Single cell experiments were performed using a test bench developed in-house. High purity feed water (18.2 MΩ cm) was circulated through both the anode and cathode compartments in separate water circuits at flow rates of 25 ml min^{-1}. Both water circuits were equipped with ion exchange resins to maintain a high degree of water purity. The cell temperature of 80 °C was reached by preheating the feed water to 75 °C and incorporating additional heating cartridges to stabilize cell temperature at all current densities. A DC power supply (TDK Lambda GEN-20-76) was used as the current source, while the cell voltages were read by a multimeter (Keithley Model 2701). A LabVIEW-based software was used to control all devices and record the data. In particular, the software ensures that no current drop occurs during a change of the operating current density, e.g., during polarization curves.

Before installation to the test bench, the cell was purged with deionized water at 80 °C for 4 h to remove potential ionic impurities. After installation to the test bench, the cell was kept hydrated at 80 °C until its dis-assembly at 1150 h. The long-term test at a current density of 2 A cm^{-2} lasted for a period of 1009 h. Before, during and after this period, electrochemical impedance spectroscopy (EIS) and polarization curves (j–E curves) were recorded. It should be noted that except for the times where EIS was recorded, the cell was never operated at cell voltages of less than 1.42 V which corresponds to the lowest voltage that was observed of the polarization curve. After 1009 h, the cell current was stopped and an additional polarization curve was recorded at 1018 h. During an extension period between 1085 h and 1150 h the current density was again set to 2 A cm^{-2}.

2.3. Electrochemical characterization

Polarization curves were plotted for the cell and EIS was performed. Specifically, polarization curves were recorded every 168 h with the DC power supply and run galvanostatically from 0.03 A cm^{-2} to 3.5 A cm^{-2}, with a limiting cell voltage of 2.2 V and 1 min hold per step. For EIS measurements the cell current had to be interrupted in order to unplug the DC power supply and connect the cell to the potentiostat (Biologic HCP 1005). EIS was run at current densities (and amplitudes) of 0.06 (0.006) − 0.11 (0.011) − 1 (0.06) − 1.5 (0.06) − 2.0 (0.06) A cm^{-2} between 100 kHz and 100 mHz, with each step being preceded by a 3 min conditioning period at the respective current density. The equivalent circuit $R_\Omega(R_{CT}Q_{DL})$ was fitted to the impedance data using Zahner's THALES software. R_Ω represents the ohmic cell resistance, R_{CT} the combined charge transfer resistance of both hydrogen and oxygen evolution reactions and Q_{DL} a constant phase element to describe the double layer capacity of the porous electrodes.

2.4. Physical and chemical characterization

Electrical through-plane resistance of the Ti-PTL were measured at room temperature with an in-house device at 0.06 A cm^{-2} and a surface pressure of 346 N cm^{-2}. For this purpose, the sample was sandwiched between and contacted by two carbon non-woven gas diffusion layers (Freudenberg FCCT KG). For cross-section imaging, a strip of the dried CCM was embedded in epoxy resin and polished. Images were recorded using a Carl Zeiss Scanning Electron Microscope (SEM) Gemini Ultra Plus. To determine the elemental distribution across the CCM, line scans were performed across the thickness of the CCM using Energy-dispersive X-ray spectroscopy (EDX). Water samples were taken weekly and the conductivity of the feed water was measured with Mettler Toledo Seven Multi. This did not increase and was below 1.2 μS cm^{-1} at all times. Imaging of the catalyst samples was performed using an FEI Tecnai F20 transmission electron microscope (TEM) with an accelerating voltage of 200 kV. For this purpose, parts of the electrode layer were scratched off the aged CCM and a fresh CCM of the same lot and then were ultrasonically dispersed in a mixture of isopropanol and water (50:50 vol.-%) and coated on a copper grid (PLANO S160). Pt particle sizes were determined on at least 400 particles per sample. X-ray diffraction (XRD) was used to determine the crystal size of the scratched off catalyst samples of the aged and a fresh CCM, respectively. XRD was performed using a STADIP transmission diffractometer with Cu-Kα1-radiation, with a wavelength of $\lambda = 1.54056$ Å. Crystal sizes were calculated using Scherrer's equation and the SiroQuant® software, version 4.

3. Results and discussion

3.1. Cell performance

Fig. 1 shows the cell voltages during the test period of 1150 h, recorded continuously (long-term, squares), during polarization curves (j−E, triangles) and during EIS (diamonds).

All voltages increase over time. In the long-term test, the increase in cell voltage was not linear and the degradation rates varied between 28 μV h^{-1} (at 150 h) and 496 μV h^{-1} (at 600 h). Up until 1009 h, the average degradation rate was 194 μV h^{-1}. After each polarization curve, the long-term voltage jumped. Upward jumps can be seen at 168, 336 and 672 h. Downward jumps occurred at 505 h and after 1009 h. Due to the jumps and the nonlinear trend, the average degradation rate cannot be used to extrapolate any future cell voltage.

Downward jumps signify a tremendous improvement in cell performance, as can be seen between 504 and 672 h. However, this phenomenon cannot be fully analyzed by EIS. Downward jumps always occur after an interruption of the cell current density, as is shown in the inset of Fig. 1. Here, the long-term voltage remains above 1.9 V until after the polarization curve is plotted. It only drops after the current interruption that occurred during the switch to the potentiostat. The following conditioning period for the impedance measurement already starts with a reduced voltage (diamond). Since the voltage did not drop to its initial value, it can be concluded that the degradation consists of both reversible and irreversible parts.

The over-time increase in cell voltage was considerably smaller during the EIS measurements (67 mV) than for long-term and j−E curves (196 and 159 mV, respectively) as the reversible parts recover before the impedance measurement. Thus, only the irreversible parts of the total degradation are detectable by means of EIS.

Reversible degradation is a fast phenomenon whose effect is more pronounced at high current densities. At the 505 h mark, a current interruption of less than 5 min was sufficient to cause a substantial recovery of 51 mV (60%) of the previously increased voltage. After a longer interruption between 1009 and 1085 h, absolute recovery was higher (119 mV), but relative recovery was similar (61%). The observed downward jumps were significantly larger at 2 A cm^{-2} than at 0.03 A cm^{-2} (59 vs. 6 mV; comparing j−E curves from 1009 to 1018 h). Thus, the amount of reversible degradation accounts for up to 61% of the total respective increase in cell voltage at 2 A cm^{-2}.

The reasons for the reversible degradation can be speculated to relate to mass transport or ohmic resistance, as these effects are generally more pronounced at higher current densities. Signs of a mass transport limitation can indeed be seen in the polarization curves after 504 h at current densities above 2 A cm^{-2} (Fig. 4a). However, no sign of mass transport limitation is seen in the EIS spectra (Fig. 3), which corresponds to the observation that the effect recovered before the EIS. The subsequent analysis of the polarization curves in Section 3.3 will indicate the reversible degradation may be related to an ohmic resistance within the cell.

Overall, the voltage at 0.03 A cm^{-2} increased by 24 mV over 1009 h, which indicates a decreased catalytic activity at the electrodes.

To find out more about the voltage increase, the trends of the half-cell potentials between 210 and 955 h are shown in Fig. 2. Both anodic and cathodic overpotential increase. The change is dominated by the anode potential, which is measured between the DHE (located on the cathode side of the membrane) and the anode
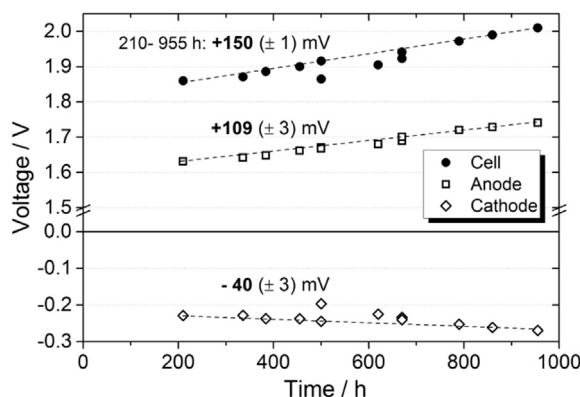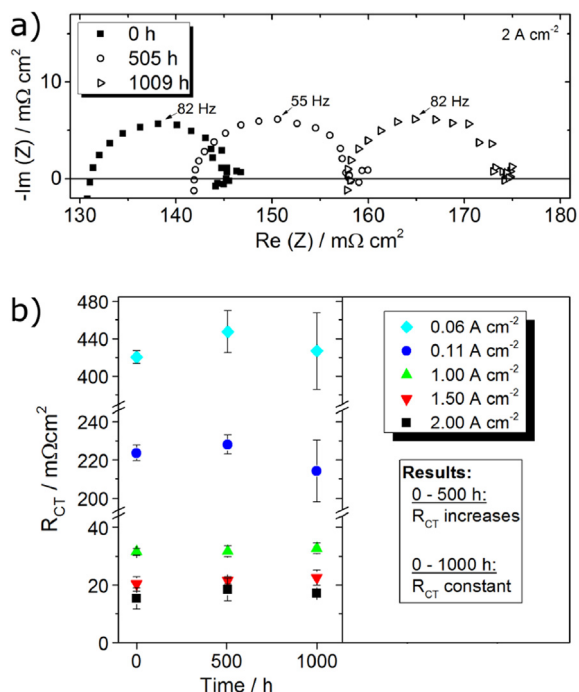

Fig. 2. Cell voltage, anode potential and cathode potential during the long-term test. Half-cell potentials are measured between the DHE and the respective bipolar plate.

Fig. 3. a) EIS spectra, recorded galvanostatically at 2 A cm^{-2} before, during and after the long-term test; b) R_{CT} at various current densities before, during and after the durability test.

bipolar plate. Possible locations of degradation therefore include the membrane, anode catalyst layer, anodic bipolar plate, Ti-PTL and all contact resistances in between. Further information regarding the location of the degradation was gained from cell impedance.

3.2. Electrochemical impedance spectroscopy (EIS)

Fig. 3a) shows the impedance spectra recorded at 2 A cm^{-2} before, during and after the durability test. All spectra consist of one semicircle. No indication of mass transport limitation exists, which would appear in form of an additional semicircle at low frequencies [29]. The fitted ohmic cell resistance increases gradually from 131 mΩ cm^2 to 157 mΩ cm^2. At the operating current density of 2 A cm^{-2}, this rise in ohmic resistance corresponds to a voltage increase of 52 mV. The increase of R_Ω over time corresponds to the findings of Rozain et al. [23] who report an increase of R_Ω over time at 80 °C and with Ti-PTL. Besides R_Ω, the charge transfer resistances R_{CT} were fitted for all spectra and are shown in Fig. 3b).

As expected from the literature [30], R_{CT} values are smaller for higher current densities. For a given current density, R_{CT} increases during the first 505 h. However, during the entire test period of 1009 h, the values remained constant within the accuracy of the fit. Therefore, the degradation of the cell performance cannot be related to R_{CT}, which combines the kinetics of both electrodes. However, it is possible that changes in the individual charge transfer resistances of the anode and cathode compensate each other. This would correspond to the rise of R_{CT} reported in the literature [23].

Using the results of EIS, we can now explain 52 of the 196 mV of increased cell voltage. However, as is known from Fig. 1 and the discussion about the reversible degradation in Section 3.1, the potentiostat only detected an increase in cell voltage by 67 mV at 2 A cm^{-2}. Of this detectable degradation, the biggest part (78%) can be explained by the increased ohmic resistance (due to membrane,
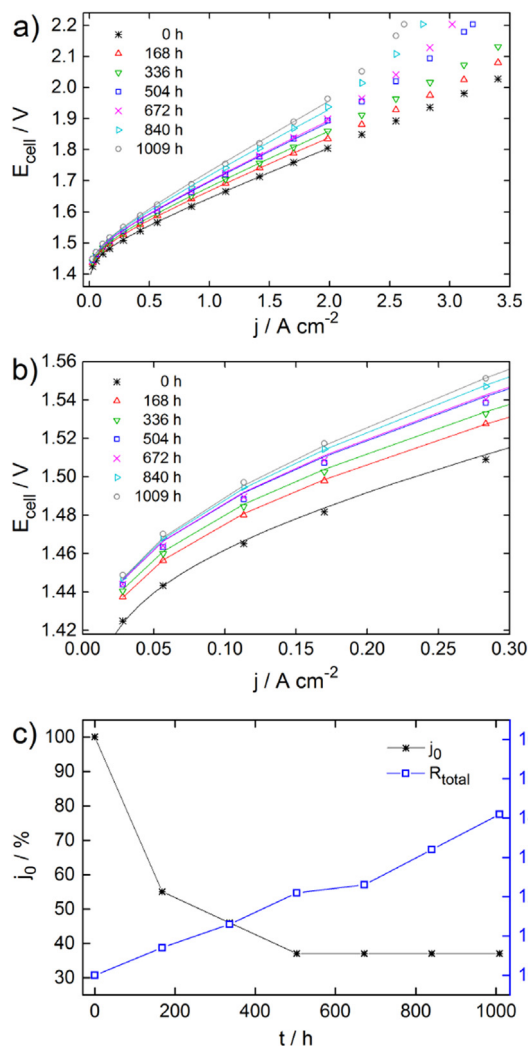
Fig. 4. a) Polarization curves; symbols = experiment, solid lines = model; b) Polarization curves in the range $0 < j < 0.3$ A cm^{-2}; symbols = experiment and solid lines = model; c) Left axis (black): Fitted values for j_0 normalized by $j_0(t = 0$ h) with lines to guide the eye. Right axis (blue): Fitted values for R_{total} normalized by $R_{total}(t = 0$ h). (For interpretation of the references to colour in this figure legend, the reader is referred to the web version of this article.)

PTL and contact resistances). In order to gain further information on the origin of the remaining degradation, the polarization curves were evaluated.

3.3. Analysis of polarization curves

Seven polarization curves were obtained during the long-term operation. These curves are analyzed on the basis of a polarization curve model which is frequently used for fuel cells and electrolyzers [31–38]. Within the model, the cell voltage is calculated based on the Nernst voltage. Kinetic and ohmic losses are added in a similar manner as described for fuel cells [37] (Eq. (1)). Within this basic approach both electrodes are combined into one effective electrode. The kinetic losses from anode and cathode are described by the Tafel Equation (Eq. (2)) through the parameter η_{act}. Eq. (2) contains the following parameters: the universal gas constant R, temperature T, Faraday's constant F, the current density j, the exchange current density j_0 and the so called symmetric factor α. It should be noted that an effective α is used which already contains the contribution of the number of electrons from the rate

determining step ($\alpha = \alpha' \cdot n$) [36].

$$E_{cell} = E_{Nernst} + \eta_{act} + j R_{total} \tag{1}$$

$$\eta_{act} = \frac{R T}{\alpha F} \ln \frac{j}{j_0} \tag{2}$$

The Nernst voltage describes the cell voltage at the conditions of thermodynamic equilibrium (zero current). It should therefore be equal for fuel cells and electrolyzers. For practical reasons, a value of $E_{Nernst} = 0.974$ V was chosen for an oxygen/hydrogen cell at ambient pressure and $T = 80\,^{\circ}$C. This value corresponds well to the experimentally observed open circuit voltage. Frequently, a different value for the Nernst voltage is chosen, though. The overall modeling results are independent of this choice. The assumption of different values for E_{Nernst} merely changes the absolute value for the exchange current density j_0 by a factor as outlined in the Appendix. The choice of a Nernst voltage of $E' = 1.183$ V would lead to a factor of $\approx 10^{-3} \cdot j_0$, but the relative change of j_0 due to degradation remains unaffected.

Eq. (1) contains two parameters that can describe degradation effects. The resistance R_{total} is a summary of all ohmic resistances from the CCM and possibly the contact resistance of PTLs. An increase in R_{total} indicates degradation of the CCM or increased contact resistance. The exchange current density j_0 is proportional to the ECSA of the catalyst [34].

The following procedure was used to fit the model parameters to the polarization curves.

1. Fitting of j_0 and α for the polarization curve at $t = 0$ h in the range of $0 < j < 0.3$ A cm^{-2}. For this purpose, η_{act} was calculated according to Eq. (3). Eq. (4) was used for a linear fit with the software GNUPLOT.

$$\eta_{act} = E_{cell} - 0.974\,\text{V} - j R_{total} \tag{3}$$

$$\eta_{act} = \frac{R T}{\alpha F} \ln j - \frac{R T}{\alpha F} \ln j_0 \tag{4}$$

The value $R_{total} = 0.131$ Ω cm^2 was drawn from EIS. It was subsequently observed that the overall ohmic resistance of the model is higher compared to the value obtained by EIS but this had very little influence on the fit (a doubling of the value of R_{total} leads to a variation of j_0 and α of less than 10%).

2. The value of α was kept constant and j_0 was fitted for all polarization curves $t > 0$ h by using a least squares algorithm. (Again, the value $R_{total} = 0.131$ Ω cm^2 was used).
3. The value of R_{total} was fitted for all polarization curves in the range $0 < j < 2.0$ A cm^{-2} by using a least squares algorithm.

The resulting fit parameters for the first polarization curve (at $t = 0$ h) are $\alpha = 1.40$, $j_0 = 3.5 \cdot 10^{-11}$ A cm^{-2} and $R_{total} = 0.147$ Ω cm^2. The quality of the fit is very good in the range of $0 < j < 2.0$ A cm^{-2}, as can be seen in Fig. 4a) and b).

The observed degradation of the cell is described by the applied model through the parameters j_0 and R_{total}. A decrease of parameter j_0 indicates decreasing electrode performance and potentially a loss of ECSA. Within the model, it is impossible to distinguish between the anode and cathode, since both electrodes are combined into one effective electrode. The relative decrease of j_0 is shown in Fig. 4c) (left axis). The relevant exchange current density decreased to about 50% of its initial value within the first 250 h. The loss in j_0 can be attributed to the anode, as the fitted values for j_0 are 11 orders of magnitude smaller than the exchange current density for hydrogen on platinum (about 1 mA cm^{-2}) [30].

The model parameter R_{total} summarizes all resistance effects, i.e., protonic and contact resistances. Fig. 4c) (right axis) shows the relative increase in total resistance over time. Resistance increases significantly with time. The slopes of R_{total} are roughly the same before the shut down event at 505 h and after the subsequent polarization curve at 672 h. The reduced slope in between indicates the value of R_{total} partially recovers during shut down. The partial recovery of increased resistance is a potential reason for the reversible degradation observed in Fig. 1. As is discernible from the half-cell potentials in Fig. 2, the main part of the performance degradation is located in the anode compartment, which suggests that the increase in R_{total} relates to the anode. As will be shown in Section 3.5.2, increased resistance at the anode is attributed to the ohmic resistance of the Ti-PTL. Therefore, the partial recovery of R_{total} (and subsequently of cell performance) potentially results from variations in the electric resistance of the Ti-PTL. These might be located in its surface layer and may be caused by, e.g., dissolution of Ti [21] during changes in electrode potential.

In the experiment, the overall degradation is observed as an increase of cell voltage at constant load operation. The results of the polarization curve model can help to separate this increase into two contributions. For operation at 2 A cm^{-2}, the model yields a 17% voltage increase caused by electrode degradation and an 83% increase arising from total resistance. The ohmic resistance clearly dominates the overall degradation. If a decrease in ECSA is responsible for the decrease in j_0, as a very rough estimate it can be said that a 10% loss of catalyst surface area leads to an increase of 3 µV h^{-1} (independent of the current density). An increase of 10% in total resistance accounts for 30 µV h^{-1} at 2 A cm^{-2}.

The identified decrease in j_0 is consistent with the constant values of R_{CT} that are found in Fig. 3. At low current densities, the slope of a polarization curve is dominated by R_{CT}. Fig. 4b) shows that this slope, and therefore R_{CT}, remain constant over time at a given current density.

The identified areas of degradation are summarized and compared to the long-term degradation in the following Section 3.4.

3.4. Overview of observed degradation

The different degradation phenomena detected by EIS and through the analysis of the polarization curves are summarized in Fig. 5. The two columns on the left side reflect the findings of Fig. 1, indicating that the degradation of the cell voltage during the long-term test can be approximated by the increase in cell voltage taken from the polarization curves (j–E) at the same current density of 2 A cm^{-2}. The middle part of Fig. 5 summarizes the identified contributions to the voltage increase and the two right columns summarize the findings of the analysis of the polarizations curves with the fit parameters j_0 and R_{total}.

It can be seen that the cell voltage at 0.03 A cm^{-2} increases by 24 mV, which coincides with the voltage increase due to a decreased exchange current density j_0 (27 mV). Furthermore, the chosen parameter R_{total} seems to include both the pure ohmic cell resistance and the reversible contribution to the voltage increase. Both the analysis of the polarization curves and the easily accessible voltage change at 0.03 A cm^{-2}, in combination with R_Ω, similarly split the voltage increase.

In the next section, the origins of the two identified areas of degradation will be localized in the cell.

3.5. Localizing the degradation

The simulation suggests that both ohmic cell resistance and
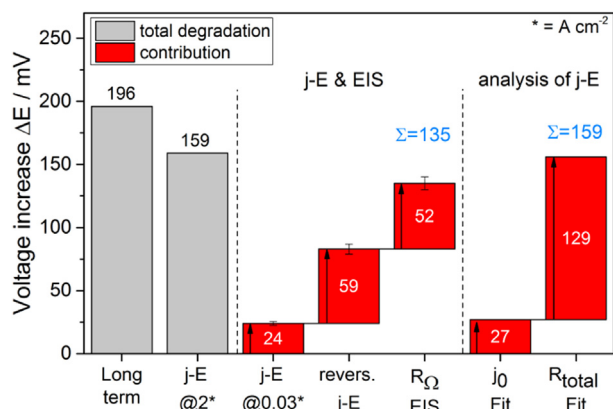
Fig. 5. Observed and analyzed degradation, summarized in a waterfall-type diagram. Grey columns: observed voltage increase during long-term test and during polarization curves (j–E), both at 2 A cm^{-2}. Identified contributions to the voltage increase are given in red columns. The voltage increase at 0.03 A cm^{-2} and the reversible voltage increase were read from the j–E curves as discussed in Section 3.1. R_Ω was analyzed by means of EIS. Parameters j_0 and R_{total} were obtained by analysis of the j–E curves in Section 3.3. (For interpretation of the references to colour in this figure legend, the reader is referred to the web version of this article.)

exchange current density degraded during the long-term test. Both factors are therefore investigated in more detail.

3.5.1. Exchange current density j_0

The analysis of the polarization curves showed a reduction in the anodic exchange current density j_0 to 37% of the initial value. One possible explanation for this drop of j_0 is a reduction of the catalyst surface area. For this reason, XRD and TEM were used to evaluate the size of the catalyst particles before and after the long-term test.

The crystal size of the anodic catalyst is 3.9 nm and remained constant during the long-term test (Table 1). Likewise, Fig. 6a) and b) do not show any changes in the morphology of the scratched off anode catalyst layer. Since the anode catalyst does not exhibit any characteristic features, no individual particle sizes can be extracted and compared.

While no change was observed for the anode catalyst, the cathodic platinum crystal sizes increased from 3.5 nm of a fresh cathode to 7.8 nm after 1150 h (Table 1). This growth is confirmed in Fig. 6 by comparing the Pt/C catalyst morphology of the fresh (c) to the aged catalyst sample (d). The catalyst particles grew and agglomerated during the test and the mean particle size of the Pt particles increases from 4.3 nm to 7.7 nm. Within the particle size distribution, the particle sizes seen in TEM correspond to the crystallite sizes determined from XRD (Table 1), which indicates that the observed Pt particles are crystalline. A less pronounced increase in Pt particle sizes was also previously reported for a short term durability test of 208 h [14]. The increased Pt particle size leads to a reduction of the available Pt surface area and will therefore reduce the cathodic exchange current density. However,

Table 1
Size of catalyst particles were investigated by two methods. The crystallite size was determined through XRD and particle size through TEM. Standard deviations of the particle size distributions are given as well.

	Anode, XRD	Cathode, XRD	Cathode, TEM
	d_{IrO_2}/nm	d_{Pt}/nm	d_{Pt}/nm
Fresh	3.9 ± 0.2	3.5 ± 0.2	4.3 ± 0.9
Aged	3.9 ± 0.2	7.8 ± 0.2	7.7 ± 2.4
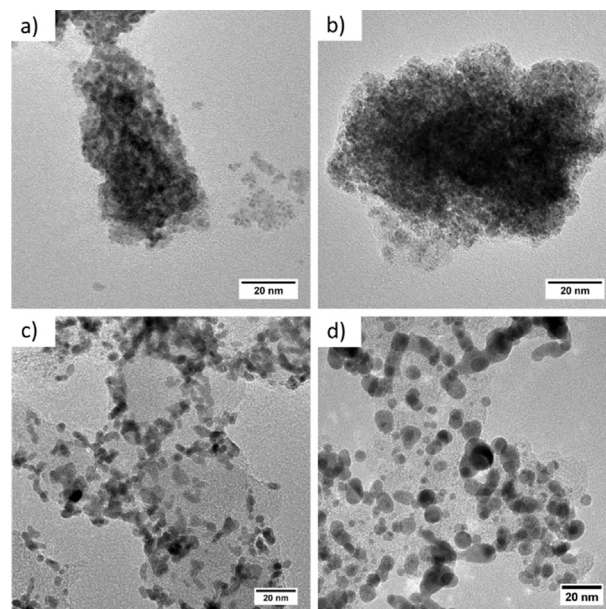
Fig. 6. TEM images of catalyst scratched off the electrodes. a) Fresh anode catalyst; b) anode catalyst after 1150 h of operation; c) fresh cathode catalyst; and d) cathode catalyst after 1150 h of operation.

the performance degradation at small current densities was shown to be caused by a reduction of the anodic exchange current density (Section 3.3). Therefore, it is unlikely that the growth of cathode Pt particles are responsible for the observed decrease in j_0.

Aside from the catalyst surface area, the exchange current density is also influenced by the protonic conductivity of the ionomer [39,40]. Kienitz et al. [39] report that cationic impurities accumulate at the cathode due to diffusion and migration. This phenomenon was confirmed for PEM water electrolysis with the contaminants Na$^+$ and Fe^{3+} [18,41]. A contaminated ionomer can lead to reduced proton concentration in the cathode, which increases the over-potential and might be seen as a lowering of the apparent exchange current density [39]. To check the CCM for cationic contaminants, embedded cross-sections of the CCM were analyzed using transversal EDX line scans.

The elements Ca, Na, Cu, Fe and Ni were not found in the CCM. However, the locations of the elements Ir, Pt and Ti are highly informative. Fig. 7 compares their distributions after 1150 h along lines from the cathode to the anode for two regions of the CCM. The region probed in Fig. 7a) was part of the passive area, that was clamped between the sealing and is therefore representative of the fresh CCM. The region probed in Fig. 7b) was part of the active area in which water electrolysis occurred and which is representative of the aged CCM. In both the fresh and aged region of the CCM, the catalyst elements Pt and Ir are only found in their respective electrodes. No indication of a platinum or iridium band within the membrane was present after 1150 h. Titanium is part of the anode catalyst and is therefore present in the anode layers of both the fresh and aged region. As expected, the fresh cathode is Ti free. Interestingly, Ti is found in the cathode of the aged area. At the working potentials of the cathode, Ti^{z+} species cannot be electrochemically reduced to metallic titanium [42], so the found Ti will exist in the cathode as an ionic species. It may therefore serve as a contaminant for the ionomer in the cathode and reduce the proton mobility, leading to an apparent reduction of the cathodic exchange current density [39,40]. However, since the decrease of j_0 was found to be related to the anode reaction, the cathode contamination with Ti species is unlikely to explain the observed decrease of j_0. Locating
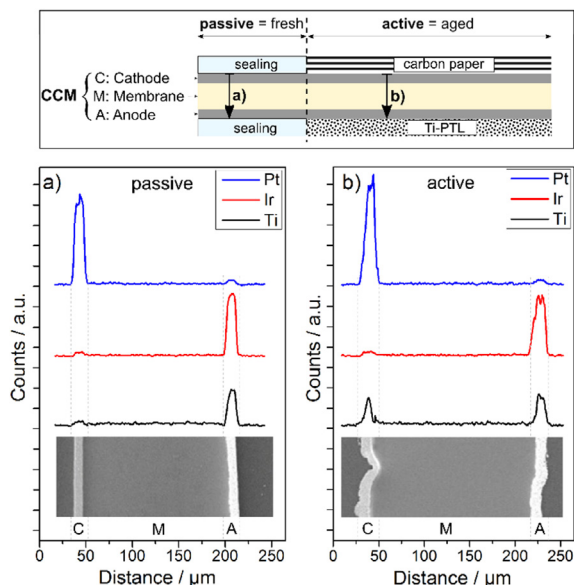
Fig. 7. Distribution of elements Ti, Ir and Pt along the cross-section of the CCM after 1150 h of operation at 2 A cm^{-2} a) passive area of CCM (under sealing); b) active area of CCM.

the origin of the Ti species can yield further information.

The test bench does not contain any Ti parts. Thus the titanium species found in the cathode layer must originate from either the bipolar plates, anode catalyst or anode Ti-PTL. The bipolar plates are made from Ti, but coated with Pt and Au. Both coatings were optically found to be without defect after the test, and so the bipolar plates can be disregarded as a Ti source. Thus, only anode components remain as potential sources of Ti (catalyst and PTL). During oxygen evolution, Ti-dissolution may occur at the titanium parts in contact with the acid polymer of the electrode [21]. It would seem that the titanium species must have migrated through the anode catalyst layer and membrane to accumulate in the cathode. Thus, in addition to the titanium that is contained in the anode catalyst, further Ti species must be present in the anode catalyst layer as contaminants. They either exchange protons with the ionomer (leading to a decrease of j_0 [39,40]) or simply change the ratio of Ir:Ti from a more active to a less active ratio. In both cases, they reduced the anode's performance and can cause the observed drop of j_0. Analytically, Ti impurities cannot be distinguished from the titanium that is part of the anode catalyst.

3.5.2. Ohmic resistance

The analysis of the polarization curves indicated a strong increase in the total resistance R_{total}. In many publications, it has been assumed that the oxidation of the Ti-PTL contributes to increasing cell resistance over time [11,13,23,43], but this hypothesis has not been validated. To investigate it, the ohmic resistance of the anode Ti-PTL was measured. It increased from 49 mΩ cm^2 at the beginning of the test to 238 mΩ cm^2 at the end. This increase proves that the ohmic resistance of the Ti-PTL is indeed a source of considerable additional resistance. Since temperature, contact pressure and current density during this ex situ measurement differ from the in situ situation, the increase in resistance can only be taken as qualitative information. To quantify the contribution of the Ti-PTL in terms of the performance degradation of the cell, we operated an additional cell that was assembled with a platinum-coated Ti-PTL.

3.6. Validation: CCM with Pt coated Ti-PTL

A fresh CCM of the identical lot was assembled using a Pt-coated Ti-PTL. The platinum coating was sputtered onto the Ti-PTL at a thickness of about 200 nm. This new cell was also operated with 2 A cm^{-2} over a duration of 380 h using the potentiostat for long-term testing and EIS recording to avoid current interruptions. The cell voltage and impedance spectra are shown in Fig. 8a).

Using a Pt-coated Ti-PTL, the cell voltage was significantly more stable than it was without the coating. Within the first 50 h the cell voltage dropped to 1.830 V and afterwards increased by only 4 mV until 380 h. This equates to a degradation rate of 12 μV h^{-1}. Within the same period, the cell in Fig. 1 (CCM from identical lot, but assembled with uncoated Ti-PTL) showed an increase in the cell voltage by 54 mV, which corresponds to 108 μV h^{-1}. Thus, the Pt coating reduced the degradation rate by 89%. The positive effect of the platinum coating can also be seen in the ohmic cell resistance. It decreases by 10 mΩ cm^2 (Pt-coated PTL) within the first 332 h instead of increasing by 28 mΩ cm^2 during the first 505 h with an uncoated Ti-PTL.

To confirm the unchanged resistance of the Pt-coated Ti-PTL, the cell resistance was measured without the CCM before and after the long-term test. Fig. 8b) shows the linear relationship between current density and voltage, indicating the ohmic resistance of the cell without CCM. Furthermore, it can be seen that the ohmic resistance of the measurement cell remained nearly unchanged over the course of the experiment, which proves the functionality of the coating.

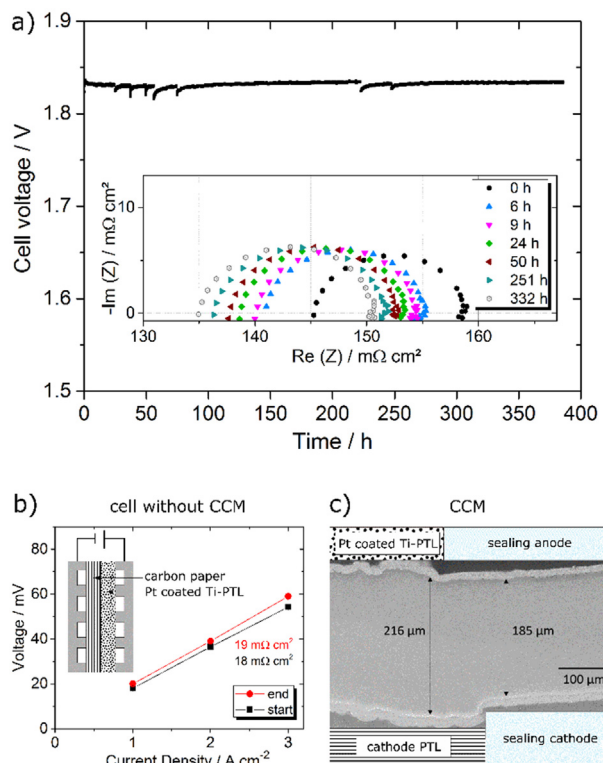The observed reduction of the ohmic resistance over time, that

Fig. 8. Long-term test over 380 h with a CCM of the same lot as was used in Fig. 1, but anodically assembled with a Pt-coated Ti-PTL. a) Cell voltage and impedance spectra during galvanostatic operation at 2 A cm^{-2}; b) Ohmic resistance of the cell when assembled without the CCM before and after the test; c) Cross-section of the CCM after the test. The left part (active region) of the CCM was clamped between the PTLs and took part in the electrolysis reaction. The right part (passive region) of the CCM was clamped between the sealing and did not take part in the reaction.

is described in Fig. 8a), may be explained by the interaction of the CCM with the PTLs. To understand this idea, Fig. 8c) shows a cross-section of the CCM at the border of the active and passive region. It can be seen that the CCM changed its shape during the long-term test. In the active region (between the PTLs), the CCM adapted the rough topology of the PTLs. This behavior was also reported for PEM fuel cells [44], as well as for the CCM assembled with regular Ti-PTL (Fig. 7). In the passive region the CCM remained flat between the smooth surface of the sealing material. We expect that the adaptation of the CCM-surface to the topology of the PTLs improves the mechanical contact and consequently decreases the contact resistance between the CCM and PTLs.

The topology change is expected to happen predominantly during the beginning of the test, as the decrease in the ohmic resistance is most pronounced during the first 50 h. Therefore, one possible deformation mechanism for this observation is creep [44,45]. Under constant mechanical stress, membrane creep occurs on the time scale of hours [46]. It can thus explain both the deformation of the membrane and the reduction of the ohmic cell resistance during the initial testing hours. A comparison of the membrane thickness in the active and passive regions shows that the final membrane thickness is dependent on the cell compression. In our cell, the compression stress appears to be higher in the sealing part. The fact that compressive stresses within the cell affect the membrane thickness must be kept in mind when potential membrane degradation is inferred solely from membrane thickness.

Concerning the cell with an uncoated Ti-PTL, the validation experiment in particular indicates that the observed trend in ohmic resistance is a superposition of at least two opposing trends: increasing cell resistance due to the passivation of the Ti-PTL can overlap with a decreasing cell resistance due to topology changes in the CCM.

4. Conclusion

In this study, we analyzed the long-term behavior of a PEM water electrolysis single cell that was operated under conventional conditions (80 °C, 2 A cm^{-2}). The average degradation rate over 1000 h was 194 μV h^{-1}. The degradation phenomena identified are increased ohmic resistance, decreased exchange current density j_0 and a reversible phenomenon that affects the evaluation of degradation mechanisms. Our findings can be summarized as follows:

- Reversible degradation accounts for up to 61% of the total voltage increase and recovers when the cell current is interrupted.
- In our setup, only irreversible degradation is visible using EIS, because the reversible contribution recovers before the impedance spectra can be recorded. Increased ohmic resistance and constant charge transfer resistance were obtained by means of EIS.
- The increased ohmic cell resistance is caused by a passivation of the anode Ti-PTL. A validation experiment with a Pt-coated Ti-PTL showed a degradation rate of only 12 μV h^{-1} within a period of 380 h and decreasing ohmic resistance during the first 332 h.
- We see a reduction of the anodic j_0, which we believe to be caused by contamination of the anode layer with Ti species.

Furthermore, we showed that the cathodic platinum particles grow during the long-term test. However, we do not believe this phenomenon to affect the stability of the cell voltage, as only anodic changes of j_0 were identified. Nevertheless, the growth of Pt particles shows that the stability of the particle size is an important issue for Pt/C catalyst development, especially in the context of reduced cathode loadings.

With this study, we contribute to a better understanding of degradation phenomena in the area of PEM water electrolysis. In particular, it is shown that degradation can originate from a variety of sources apart from the CCM, which in our case showed high stability.

Appendix A

A1: Effect of the choice of standard voltage

The modeling approach uses Eq. (5) in order to describe the polarization curve.

$$E_{cell} = E_{Nernst} + \frac{R\,T}{\alpha\,F} \ln \frac{j}{j_0} + j\,R_{total} \tag{5}$$

Within this work a value of $E_{Nernst} = 0.974$ V was obtained by taking into account the solubility of oxygen and hydrogen in water. In other works the value of $E° = 1.183$ V is used instead (depending on the underlying assumptions). The results of the modeling are independent of this choice. The assumption of different values for E_{Nernst} (or $E°$ respectively) merely changes the values for the exchange current density j_0 by a factor of β, since each model must describe the experimental polarization curve. The magnitude of β is derived in Eqs. (6)–(8).

$$E_{cell} = E_{Nernst} + \frac{R\,T}{\alpha\,F} \ln \frac{j}{j_0\,\beta} + j\,R_{total} \tag{6}$$

$$E_{cell} = E_{Nernst} + \frac{R\,T}{\alpha\,F} \left(\ln(j) - \ln(j_0) - \ln(\beta) \right) + j\,R_{total} \tag{7}$$

$$E_{cell} = E_{Nernst} - \frac{R\,T}{\alpha\,F} \ln\beta + \frac{R\,T}{\alpha\,F} \ln \frac{j}{j_0} + j\,R_{total} \tag{8}$$

Now, the effectively used Nernst voltage E' can be described according to Eq. (9).

$$E' = E_{Nernst} - \frac{R\,T}{\alpha\,F} \ln\beta \tag{9}$$

Therefore, the value of β is obtained by Eq. (10).

$$\beta = \exp\left(\frac{\alpha\,F}{R\,T} \left(E_{Nernst} - E' \right) \right) \tag{10}$$

The choice of a Nernst voltage of $E' = 1.183$ V (with T = 453 K and $\alpha = 1.29$) would lead to a factor of $\beta = 10^{-3}$.

A2: Fitted polarization curves

Fig. 4b) shows the resulting fit from step 2 of the fitting procedure in the range of $0 < j < 0.3$ A cm^{-2}. The resulting polarization curves after step 3 are shown in Fig. 4a). The fit shows a good quality within the range of $0 < j < 2$ A cm^{-2}. A pronounced

deviation from the linear trend can be observed for curves after 500 h at very high current densities $j > 2$ A cm^{-2}. This effect can not be described by the model.

References

[1] M. Carmo, D.L. Fritz, J. Mergel, D. Stolten, A comprehensive review on PEM water electrolysis, Int. J. Hydrogen Energy 38 (12) (2013) 4901–4934.

[2] Energiepark Mainz, Green light for green hydrogen at Energiepark Mainz (02.07.2015). URL www.siemens.com/press/pool/de/feature/2014/corporate/2014-05-energiepark-mainz/pr2015070276pden.pdf.

[3] K.E. Ayers, J.N. Renner, N. Danilovic, J.X. Wang, Y. Zhang, R. Maric, H. Yu, Pathways to ultra-low platinum group metal catalyst loading in proton exchange membrane electrolyzers, Catal. Today 262 (2016) 121–132.

[4] H.-Y. Jung, S.-Y. Huang, B.N. Popov, High-durability titanium bipolar plate modified by electrochemical deposition of platinum for unitized regenerative fuel cell (URFC), J. Power Sources 195 (7) (2010) 1950–1956.

[5] A.S. Gago, S.A. Ansar, B. Saruhan, U. Schulz, P. Lettenmeier, N.A. Cañas, P. Gazdzicki, T. Morawietz, R. Hiesgen, J. Arnold, K.A. Friedrich, Protective coatings on stainless steel bipolar plates for proton exchange membrane (PEM) electrolysers, J. Power Sources 307 (2016) 815–825.

[6] N.K. Kuromoto, R.A. Simão, G.A. Soares, Titanium oxide films produced on commercially pure titanium by anodic oxidation with different voltages, Mater. Charact. 58 (2) (2007) 114–121.

[7] Y.-T. Sul, C.B. Johansson, Y. Jeong, T. Albrektsson, The electrochemical oxide growth behaviour on titanium in acid and alkaline electrolytes, Med. Eng. Phys. 23 (5) (2001) 329–346.

[8] S.-H. Wang, J. Peng, W.-B. Lui, J.-S. Zhang, Performance of the gold-plated titanium bipolar plates for the light weight PEM fuel cells, J. Power Sources 162 (1) (2006) 486–491.

[9] H.-Y. Jung, S.-Y. Huang, P. Ganesan, B.N. Popov, Performance of gold-coated titanium bipolar plates in unitized regenerative fuel cell operation, J. Power Sources 194 (2) (2009) 972–975.

[10] S.A. Grigoriev, P. Millet, S.V. Korobtsev, V.I. Porembskiy, M. Pepic, C. Etievant, C. Puyenchet, V.N. Fateev, Hydrogen safety aspects related to high-pressure polymer electrolyte membrane water electrolysis, Int. J. Hydrogen Energy 34 (14) (2009) 5986–5991.

[11] E. Rasten, G. Hagen, R. Tunold, Electrocatalysis in water electrolysis with solid polymer electrolyte, Electrochim. Acta 48 (25–26) (2003) 3945–3952.

[12] L. Ma, S. Sui, Y. Zhai, Investigations on high performance proton exchange membrane water electrolyzer, Int. J. Hydrogen Energy 34 (2) (2009) 678–684.

[13] M. Kondoh, N. Yokoyama, C. Inazumi, Development of solid polymer-electrolyte water electrolyser, J. New Mater. Electrochem. Syst. 3 (2000) 61–65.

[14] G. Wei, Y. Wang, C. Huang, Q. Gao, Z. Wang, L. Xu, The stability of MEA in SPE water electrolysis for hydrogen production, Int, J. Hydrogen Energy 35 (9) (2010) 3951–3957.

[15] S. Sun, Z. Shao, H. Yu, G. Li, B. Yi, Investigations on degradation of the long-term proton exchange membrane water electrolysis stack, J. Power Sources 267 (2014) 515–520.

[16] P. Millet, R. Ngameni, S.A. Grigoriev, N. Mbemba, F. Brisset, A. Ranjbari, C. Etiévant, PEM water electrolyzers: from electrocatalysis to stack development, Int. J. Hydrogen Energy 35 (10) (2010) 5043–5052.

[17] F. Andolfatto, R. Durand, A. Michas, P. Millet, P. Stevens, Solid polymer electrolyte water electrolysis: electrocatalysis and long-term stability, Int. J. Hydrogen Energy 19 (5) (1994) 421–427.

[18] X. Wang, L. Zhang, G. Li, G. Zhang, Z.-G. Shao, B. Yi, The influence of Ferric ion contamination on the solid polymer electrolyte water electrolysis performance, Electrochim. Acta 158 (2015) 253–257.

[19] T. Okada, S. Møller-Holst, O. Gorseth, S. Kjelstrup, Transport and equilibrium properties of Nafion membranes with H$^+$ and Na$^+$ ions, J. Chem. Phys. 442 (1–2) (1998) 137–145.

[20] T. Okada, Y. Ayato, J. Dale, M. Yuasa, I. Sekine, O. Andreas Asbjørnsen, Oxygen reduction kinetics at platinum electrodes covered with perfluorinated ionomer in the presence of impurity cations Fe^{3+}, Ni^{2+} and Cu^{2+}, Phys. Chem. Chem. Phys. 2 (14) (2000) 3255–3261.

[21] S. Cherevko, T. Reier, A.R. Zeradjanin, Z. Pawolek, P. Strasser, K.J. Mayrhofer, Stability of nanostructured iridium oxide electrocatalysts during oxygen evolution reaction in acidic environment, Electrochem. Commun. 48 (2014) 81–85.

[22] S. Cherevko, S. Geiger, O. Kasian, N. Kulyk, J.-P. Grote, A. Savan, B.R. Shrestha,

[23] S. Merzlikin, B. Breitbach, A. Ludwig, K.J. Mayrhofer, Oxygen and hydrogen evolution reactions on Ru, RuO2, Ir, and IrO2 thin film electrodes in acidic and alkaline electrolytes: a comparative study on activity and stability, Catal. Today 262 (2015) 170–180.

[23] C. Rozain, E. Mayousse, N. Guillet, P. Millet, Influence of iridium oxide loadings on the performance of PEM water electrolysis cells: part II – advanced oxygen electrodes, Appl. Catal. B 182 (2016) 123–131.

[24] E. Brightman, J. Dodwell, N. van Dijk, G. Hinds, In situ characterisation of PEM water electrolysers using a novel reference electrode, Electrochem. Commun. 52 (2015) 1–4.

[25] J. Giner, A practical reference electrode, J. Electrochem. Soc. 111 (3) (1964) 376.

[26] J.H. Ohs, U. Sauter, S. Maass, D. Stolten, The effect of the reference electrode position on the measurement of half cell polarization in proton-exchange membrane fuel cells, J. Electrochem. Soc. 159 (7) (2012) F181–F186.

[27] Z. Siroma, R. Kakitsubo, N. Fujiwara, T. Ioroi, S.-I. Yamazaki, K. Yasuda, Compact dynamic hydrogen electrode unit as a reference electrode for PEMFCs, J. Power Sources 156 (2) (2006) 284–287.

[28] M. Carmo, T. Roepke, F. Scheiba, C. Roth, S. Moeller, H. Fuess, J.G. Poco, M. Linardi, The use of a dynamic hydrogen electrode as an electrochemical tool to evaluate plasma activated carbon as electrocatalyst support for direct methanol fuel cell, Mater. Res. Bull. 44 (1) (2009) 51–56.

[29] I. Dedigama, P. Angeli, K. Ayers, J.B. Robinson, P.R. Shearing, D. Tsaoulidis, D. Brett, In situ diagnostic techniques for characterisation of polymer electrolyte membrane water electrolysers – flow visualisation and electrochemical impedance spectroscopy, Int, J. Hydrogen Energy 39 (9) (2014) 4468–4482.

[30] C. Rozain, P. Millet, Electrochemical characterization of polymer electrolyte membrane water electrolysis cells, Electrochim. Acta 131 (2014) 160–167.

[31] P. Choi, D.G. Bessarabov, R. Datta, A simple model for solid polymer electrolyte (SPE) water electrolysis, Solid State Ionics 175 (2004) 535.

[32] F. Marangio, M. Santarelli, M. Calì, Theoretical model and experimental analysis of a high pressure PEM water electrolyser for hydrogen production, Int. J. Hydrogen Energy 34 (2009) 1143.

[33] H. Su, V. Linkov, B.J. Bladergroen, Membrane electrode assemblies with low noble metal loadings for hydrogen production from solid polymer electrolyte water electrolysis, Int. J. Hydrogen Energy 38 (23) (2013) 9601–9608.

[34] D. Bezmalinovic, B. Simic, F. Barbir, Characterization of PEM fuel cell degradation by polarization change curves, J. Power Sources 294 (2015) 82–87.

[35] U. Reimer, B. Schumacher, W. Lehnert, Accelerated degradation of high-temperature polymer electrolyte fuel cells: discussion and empirical modeling, J. Electrochem. Soc. 162 (2015). F153.

[36] F. Barbir, PEM Fuel Cells, Elsevier, Amsterdam, Boston, Heidelberg, 2005.

[37] R.P. O'Hayre, S.-W. Cha, W.G. Colella, F.B. Prinz, Fuel Cell Fundamentals, second ed., Wiley, New York, 2009.

[38] M. Eikerling, A.A. Kulikovsky (Eds.), Polymer Electrolyte Fuel Cells, CRC Press, Boca Raton, London, New York, 2015.

[39] B.L. Kienitz, H. Baskaran, T.A. Zawodzinski, Modeling the steady-state effects of cationic contamination on polymer electrolyte membranes, Electrochim. Acta 54 (6) (2009) 1671–1679.

[40] B. Kienitz, H. Baskaran, T. Zawodzinski, B. Pivovar, A Half Cell Model to Study Performance Degradation of a PEMFC due to Cationic Contamination, in: 212th ECS Meeting, October 7-October 12, 2007, pp. 777–788.

[41] L. Zhang, X. Jie, Z.-G. Shao, X. Wang, B. Yi, The dynamic-state effects of sodium ion contamination on the solid polymer electrolyte water electrolysis, J. Power Sources 241 (2013) 341–348.

[42] P. Vanýsek, Electrochemical series, in: W.M. Haynes, D.R. Lide, T.J. Bruno (Eds.), CRC Handbook of Chemistry and Physics, CRC, Boca Raton and Fla and London, 2012, pp. 5–80.

[43] S.P.S. Badwal, S. Giddey, F.T. Ciacchi, Hydrogen and oxygen generation with polymer electrolyte membrane (PEM)-based electrolytic technology, Ionics 12 (1) (2006) 7–14.

[44] V. Stanic, M. Hoberecht, Mechanism of pinhole formation in membrane electrode assemblies for PEM fuel cells, in: M. Murthy (Ed.), Proton Conducting Membrane Fuel Cells IV, Vol. V. 2004-21 of Proceedings, Electrochemical Society, Pennington and NJ, 2006, p. 391.

[45] P.W. Majsztrik, A.B. Bocarsly, J.B. Benziger, Viscoelastic response of nafion. Effects of temperature and hydration on tensile creep, Macromolecules 41 (24) (2008) 9849–9862.

[46] A. Sadeghi Alavijeh, R.M. Khorasany, A. Habisch, G.G. Wang, E. Kjeang, Creep properties of catalyst coated membranes for polymer electrolyte fuel cells, J. Power Sources 285 (2015) 16–28.